Supplementary Information for

Maximizing interface stability in all-solid-state lithium batteries through entropy stabilization and fast kinetics

Xiangkun Kong[1,2], Run Gu[1,2], Zongzi Jin[1,2], Lei Zhang[1,2], Chi Zhang[1,2], Wenyi Xiang[1,2], Cui Li[1,2], Kang Zhu[2], Yifan Xu[1,2], Huang Huang[1,2], Xiaoye Liu[1,2], Ranran Peng[1,2], Chengwei Wang[1,2]*

1. Key Laboratory of Precision and Intelligent Chemistry, University of Science and Technology of China, Hefei, Anhui, 230026, China.

2. Department of Materials Science and Engineering, University of Science and Technology of China, Hefei, Anhui, 230026, China.

Email: vcwang@ustc.edu.cn

Keywords: Ultrafast sintering, All-solid-state Li batteries, High-entropy cationic disordered rock salt positive electrodes, Positive electrode|Electrolyte interface

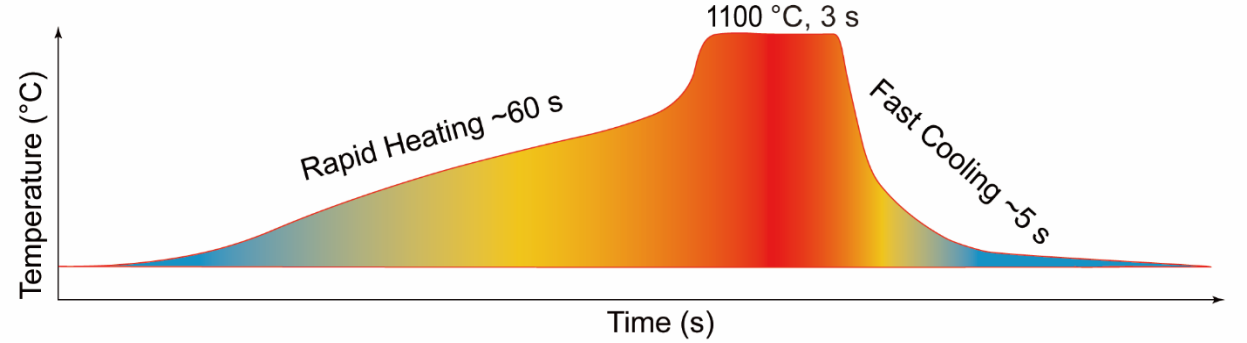

Supplementary Figure 1. The rise and fall curves of the HE-DRXs are synthesized in one step. The reactor was heated from room temperature to the targeted temperature within ~ 60 s, followed by isothermal sintering for approximately 3 s and rapid cooling for 5 s.

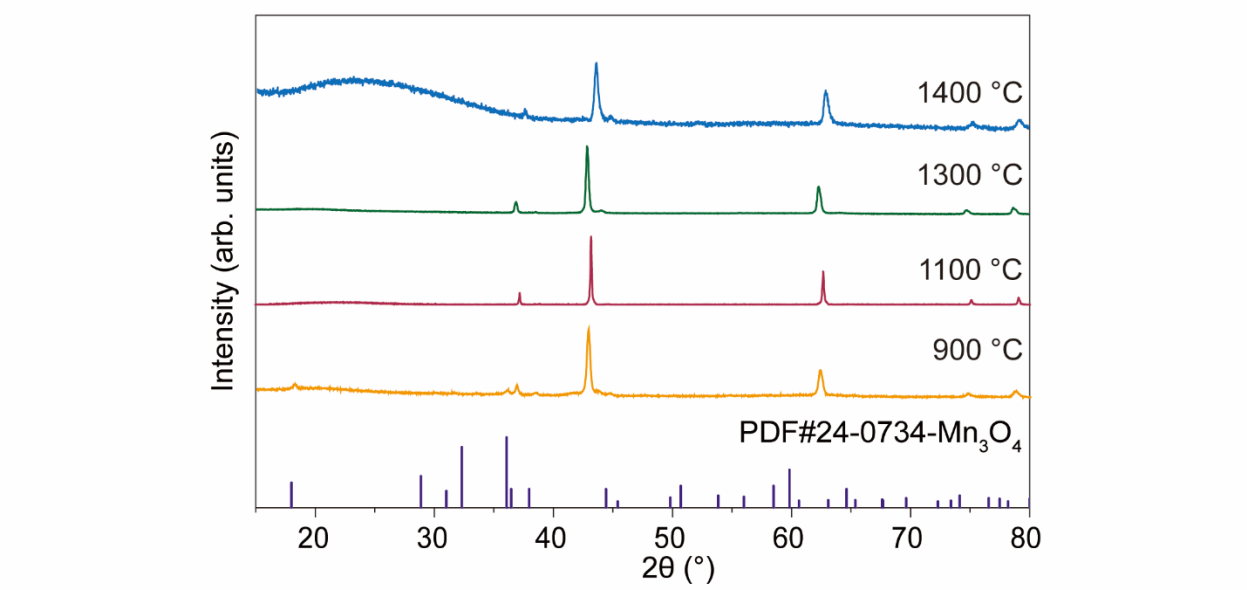

Supplementary Figure 2. XRD patterns of HE-DRXs synthesized at different temperatures by UHS.

To investigate the optimal synthesis conditions of the HE-DRXs, precursor powders were sintered at different temperatures (900 ℃, 1100 ℃, 1300 ℃, and 1400 ℃). X-ray diffraction (XRD) shows that a small amount of Mn_2O_3 exists in HE-DRXs at 900 ℃. The precursor powders are completely converted to a single phase without any obvious impurity peaks when the reaction temperature is between 1100 ℃ and 1300 ℃.

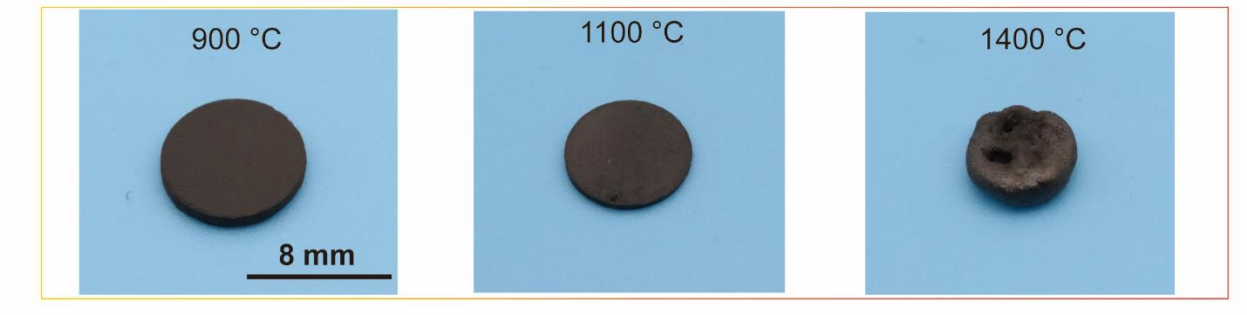

Supplementary Figure 3. Photographs of HE-DRXs synthesized at different temperatures.

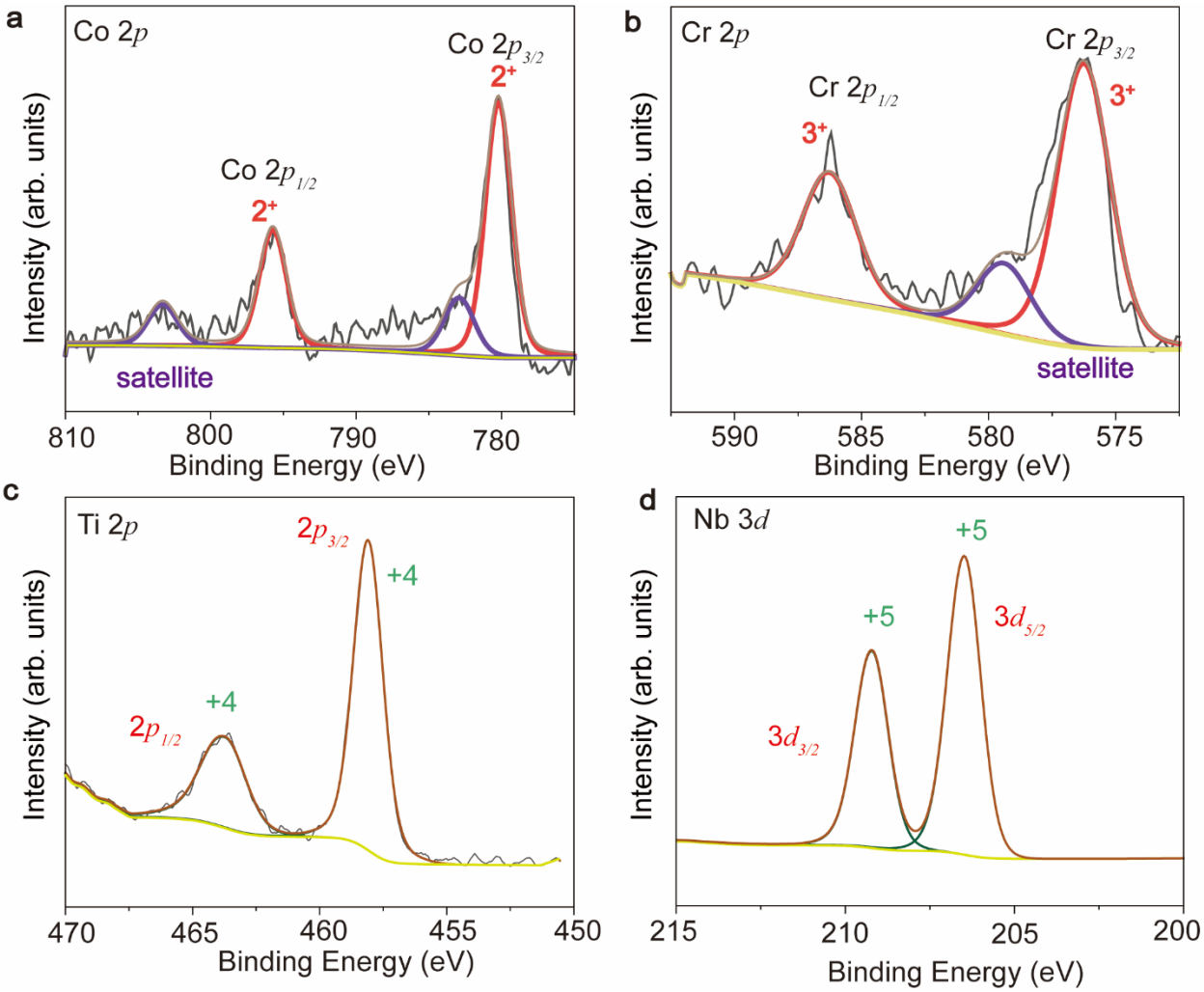

Supplementary Figure 4. XPS spectra of (a) Co2p, (b) Cr 2p, (c) Ti 2p, (d) Nb 3d of the HE-DRXs.

Supplementary Table 1. Target versus measured atomic ratios of the as-synthesized materials.

Element	Measured element content W(%)	Measured ratio	Target atomic ratio
Li	9.04%	1.30	1.30
Ti	4.60%	0.10	0.10
Cr	5.81%	0.11	0.10
Mn	11.72%	0.21	0.20
Co	6.28%	0.11	0.10
Nb	18.66%	0.20	0.20

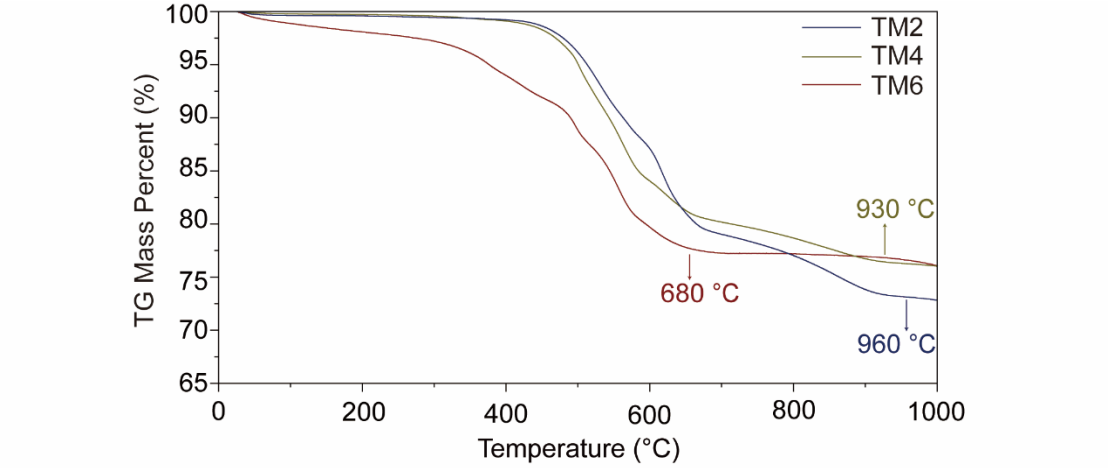

Supplementary Figure 5. TG curves for the precursor mass of TM2, TM4 and TM6.

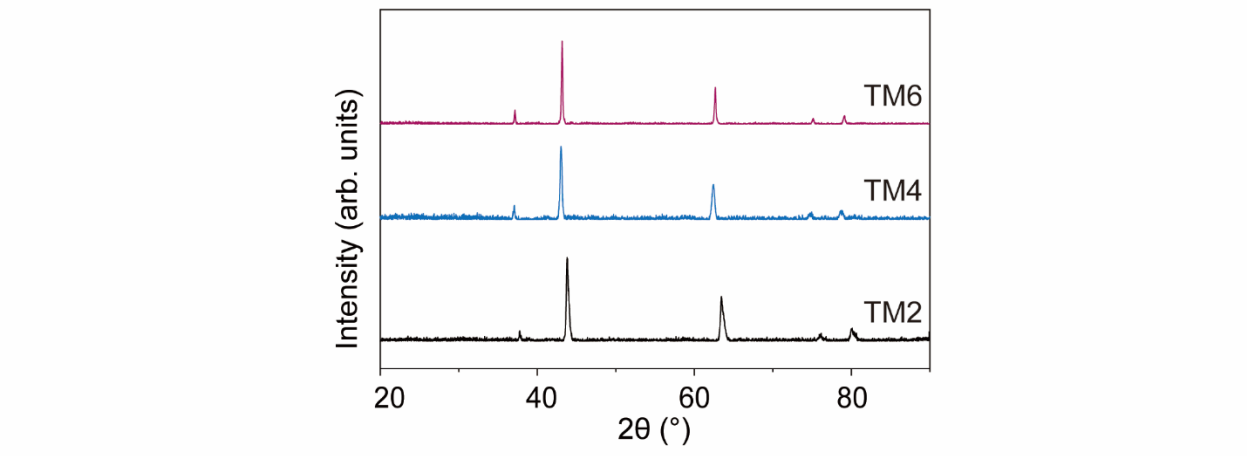

Supplementary Figure 6. XRD patterns of TM2, TM4 and TM6 were synthesized by UHS at 1150 ℃ for 10 s.

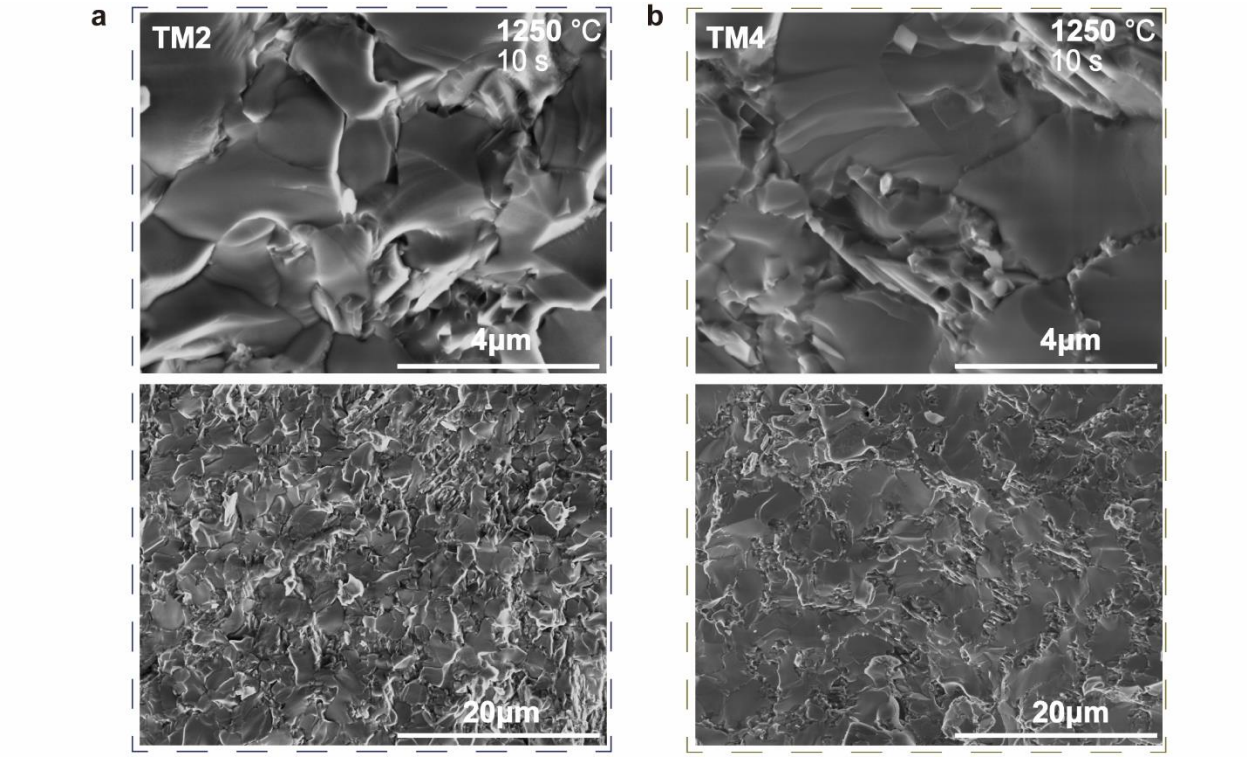

Supplementary Figure 7. SEM images of TM2(a) and TM4(b) reacted and sintered at 1250 ℃ for 10 s.

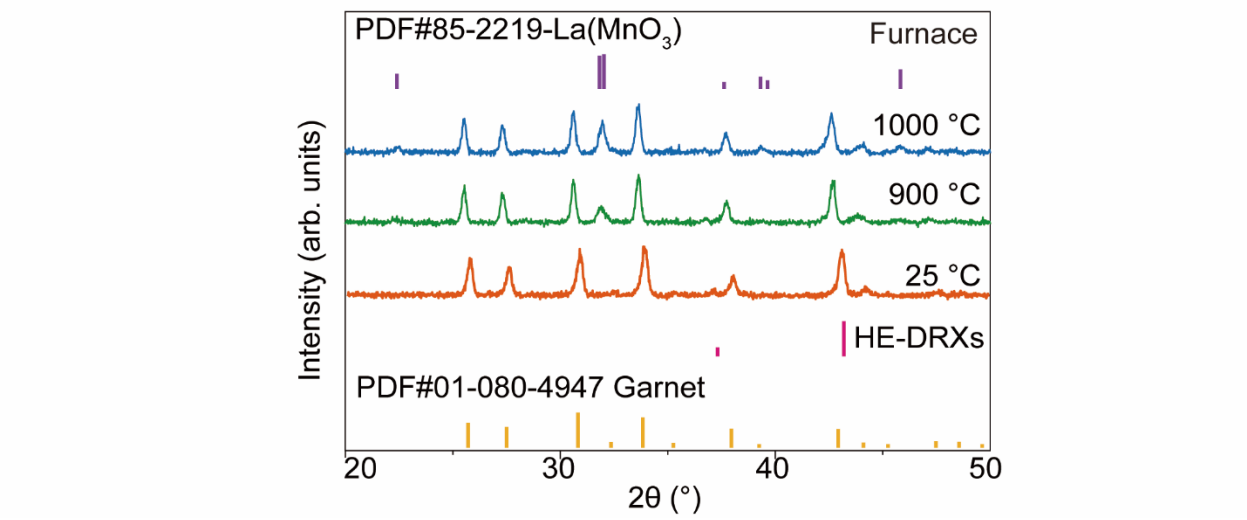

Supplementary Figure 8. XRD patterns of LLZTO and HE-DRXs at 900 ℃ and 1100 ℃ at a heating rate of 10 ℃/min.

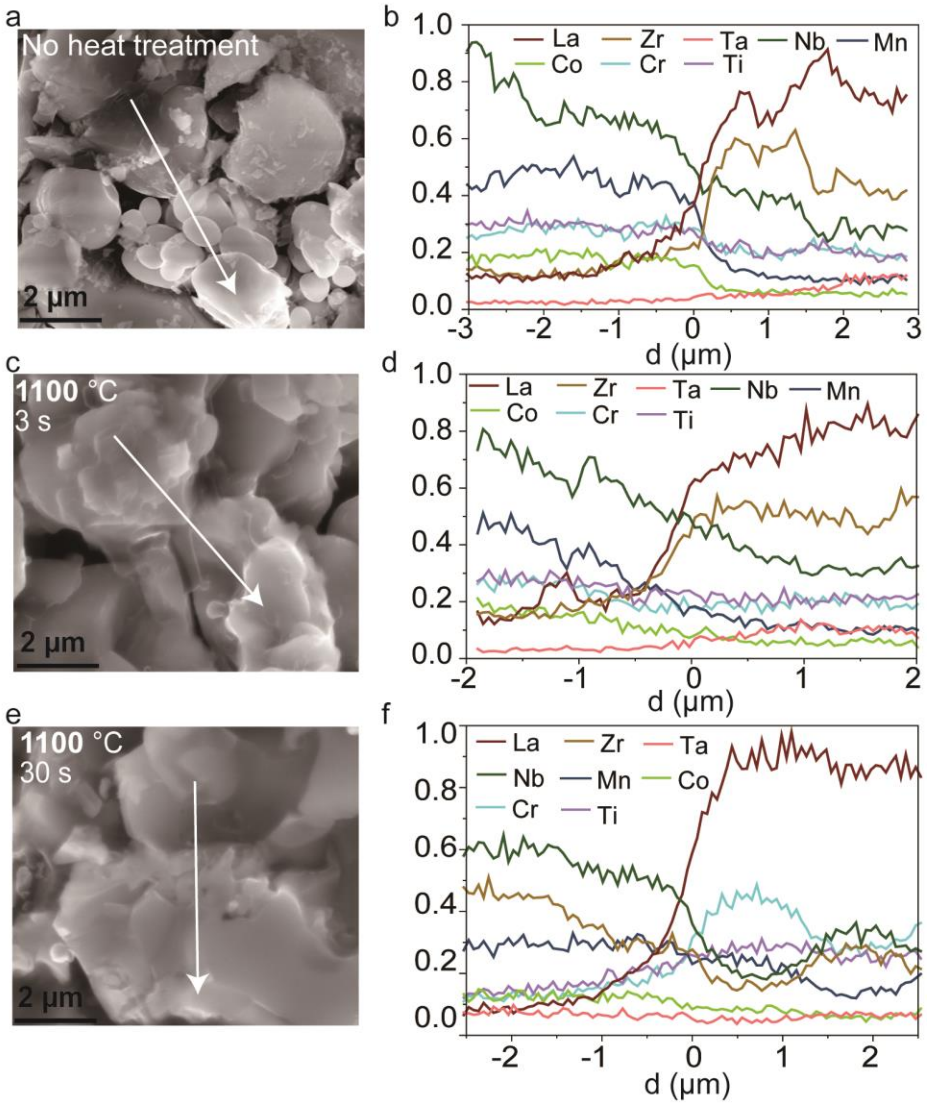

Supplementary Figure 9. EDS line profiles of the TM6 and LLZTO before (a, b) and after heating treatment at 1100 ℃ for 3 s (c, d) and (e, f).

SEM/EDS line profiles showed that the mixed powder of TM6 and LLZTO particles without heat treatment exhibited a dispersed distribution. After heating treatment at 1100 ℃ for 3 s, a notable improvement in bonding between TM6 and LLZTO particles was observed and EDS Line profiles further showed that there was no element diffusion between TM6 and LLZTO after heat treatment. After heating treatment at 1100 ℃ for 30 s, the elements of TM6 and LLZTO become interdiffusion.

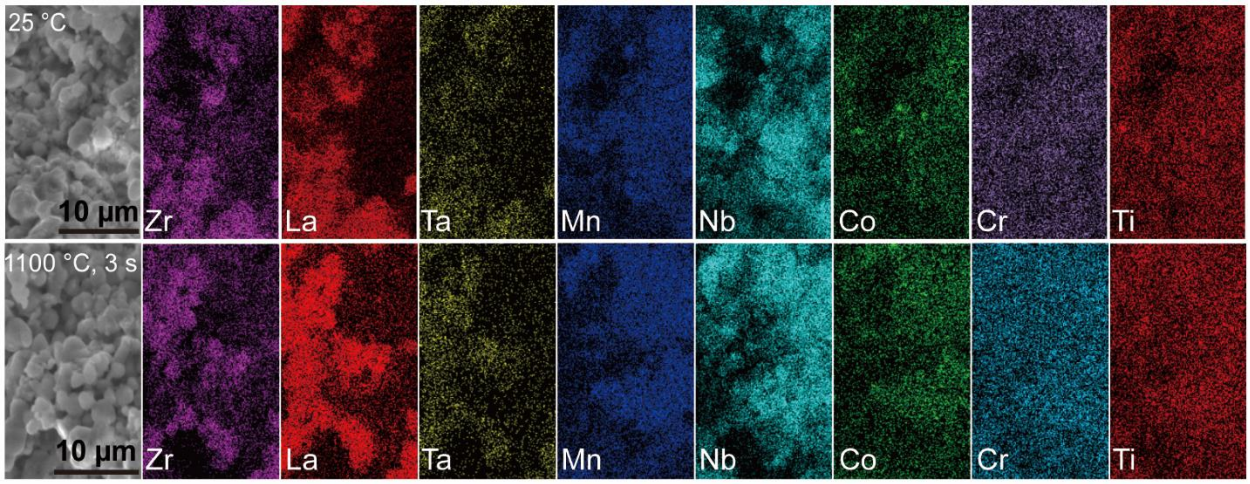

Supplementary Figure 10. EDS diagrams of the HE-DRXs and LLZTO before and after heat treatment.

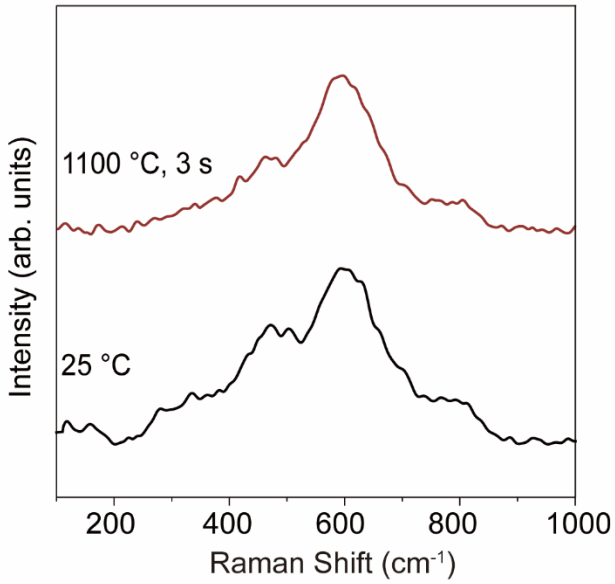

Supplementary Figure 11. Raman spectra of the HE-DRXs and LLZTO before and after heat treatment.

The Raman spectra of the LLZTO and TM6 are consistent with those of the mixture before heating treatment.

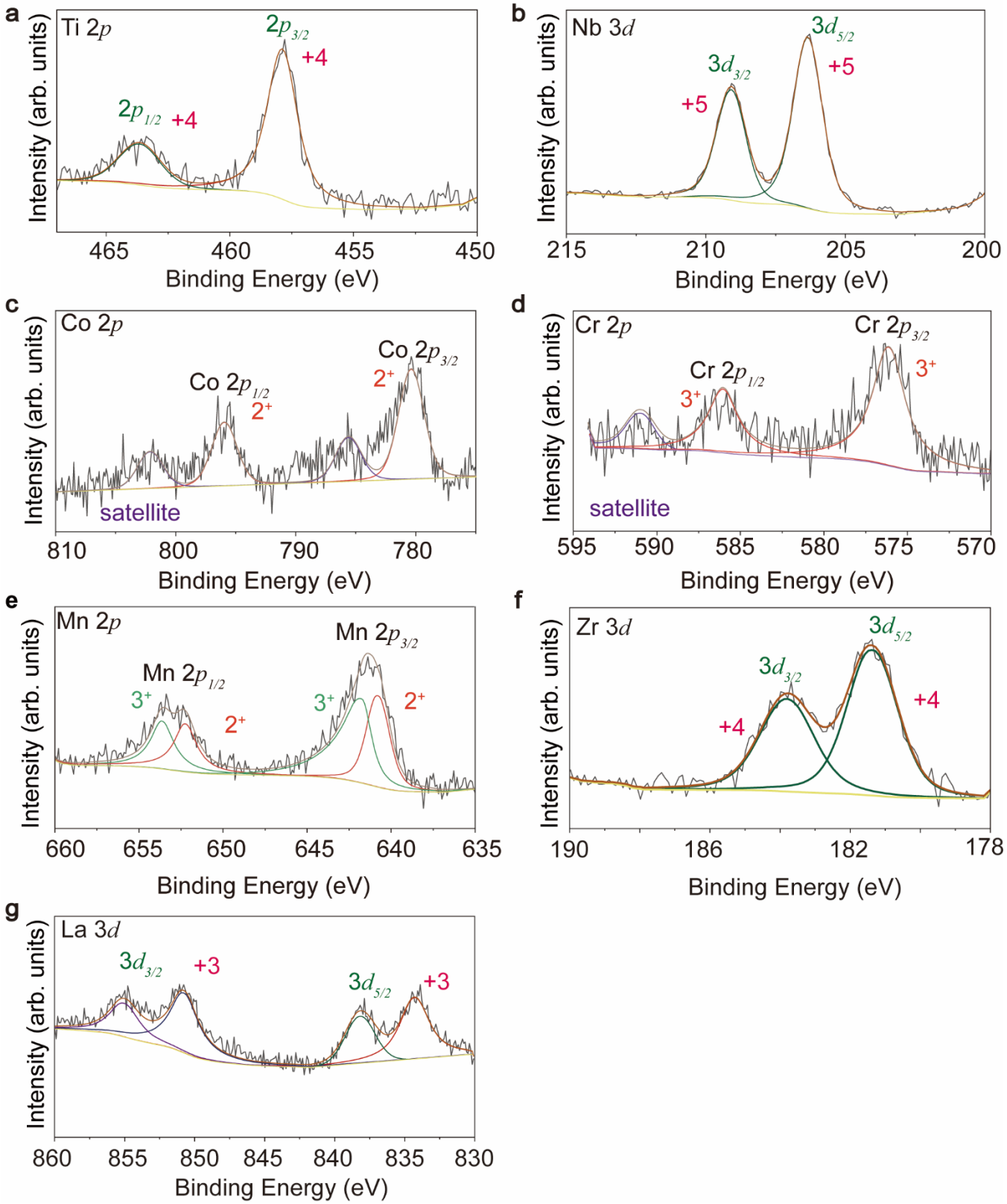

Supplementary Figure 12. XPS spectra of (a) Ti 2p, (b) Nb 3d, (c) Co2p, (d) Cr 2p, (e) Mn 2p, (f) Zr 3d and (g) La 3d of TM6 and LLZTO after heat treatment at 1100 ℃ for 3 s by UHS.

The valence states of Mn are both +2 and +3, Co is in the +2 oxidation state and Cr is in the +3 oxidation state. Ti and Nb exhibit valence states of +4 and +5, respectively. The valence states of La and Zr maintain the designed valence states, indicating relatively stable.

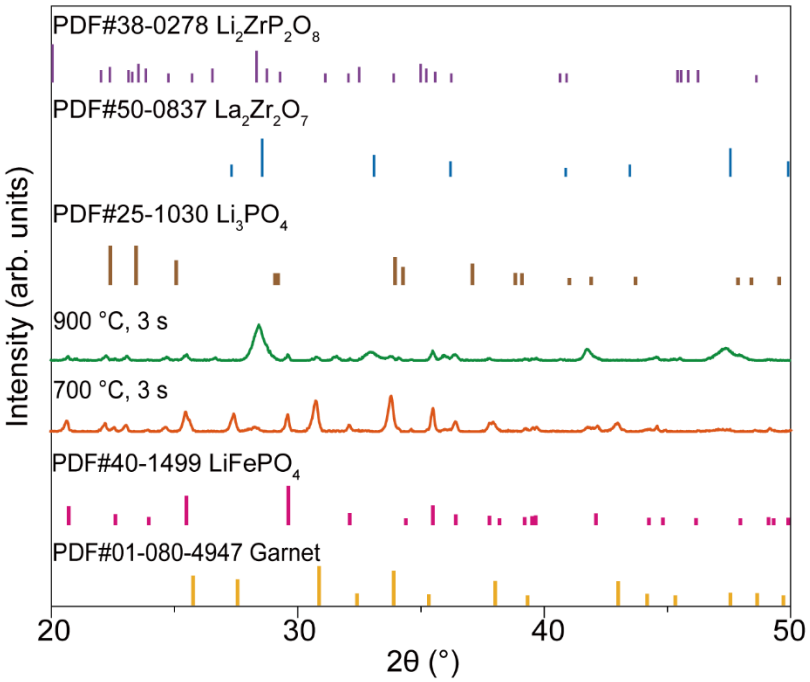

Supplementary Figure 13. XRD patterns of LLZTO and $LiFePO_4$ heated by UHS. The XRD patterns indicate that $LiFePO_4$ does not react with LLZTO at 700 ℃ for 3 s. However, a violent reaction occurs resulting in the formation of impurity phases including Li_3PO_4, La_2ZrO_7 and $Li_2ZrP_2O_8$ at 900 ℃.

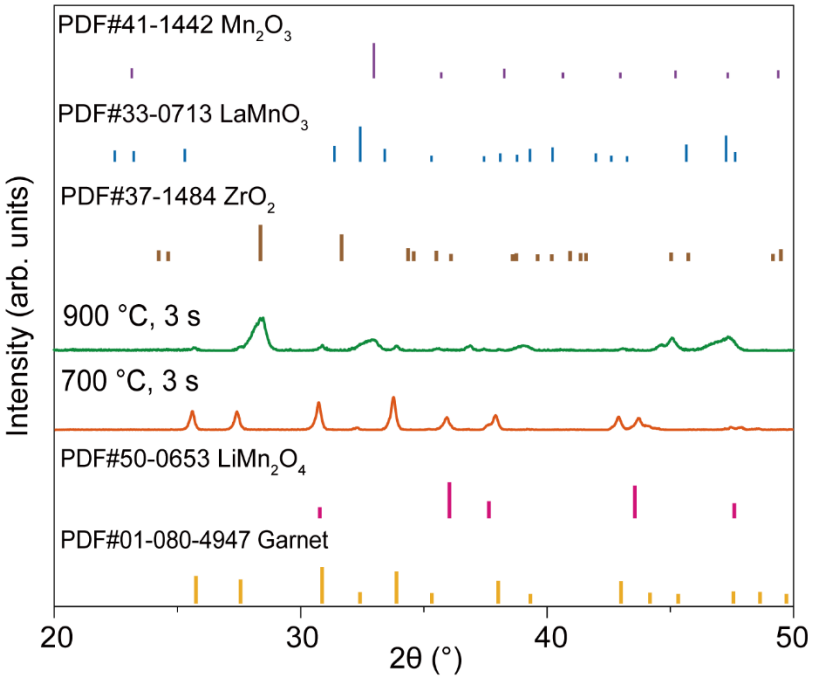

Supplementary Figure 14. XRD patterns of LLZTO and $LiMn_2O_4$ heated by UHS. $LiMn_2O_4$ does not react with LLZTO at 700℃ for 3 s, while the spinel structure disappears and impurity phases ($LaMnO_3$, ZrO_2 and Mn_2O_3) are formed at 900 ℃.

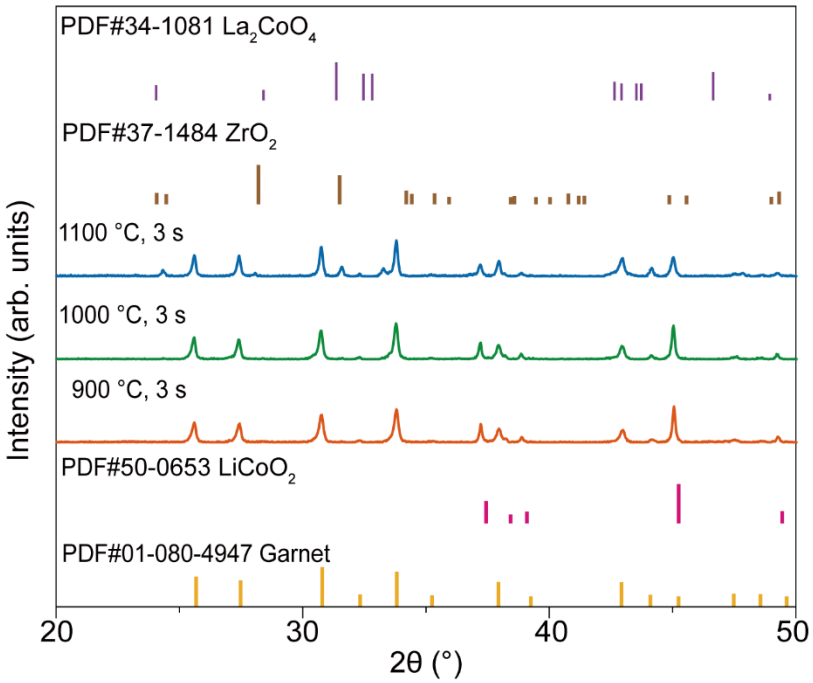

Supplementary Figure 15. XRD patterns of LLZTO and $LiCoO_2$ heated by UHS. $LiCoO_2$ and

LLZTO can be stabilized at 1000 ℃ for 3 s, but the side reaction is obvious at 1100 ℃, and La_2CoO_4 and ZrO_2 are formed.

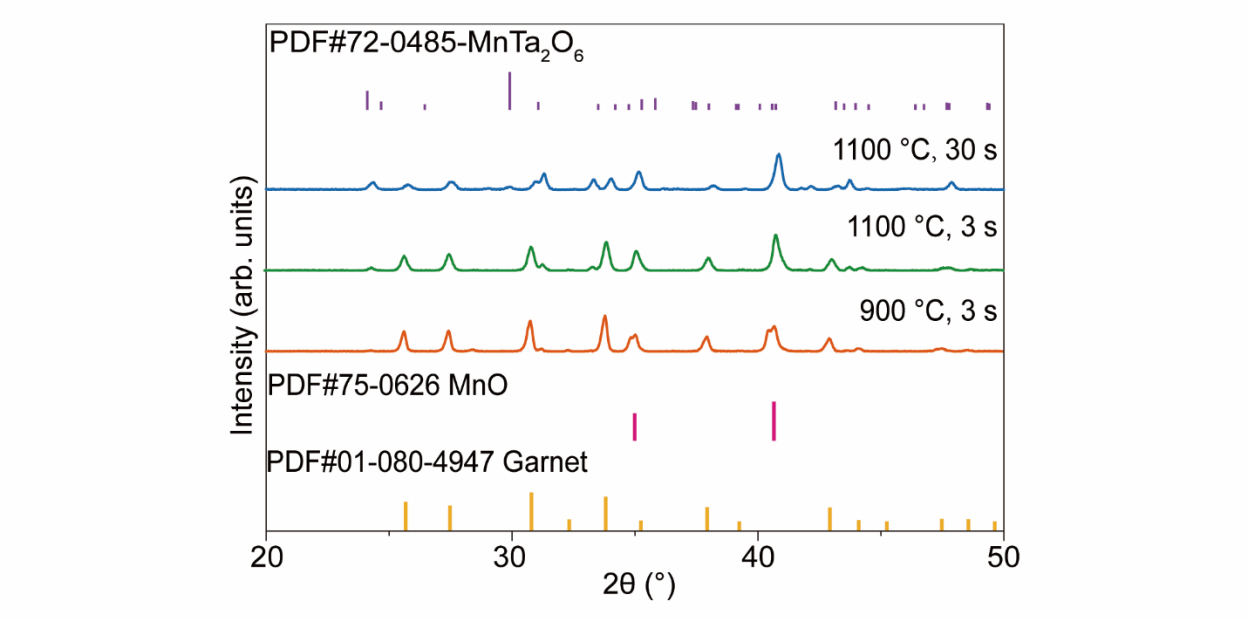

Supplementary Figure 16. XRD patterns of LLZTO and MnO heated by UHS. The XRD patterns indicate that MnO and LLZTO are stable at 1100 ℃ for 3 s.

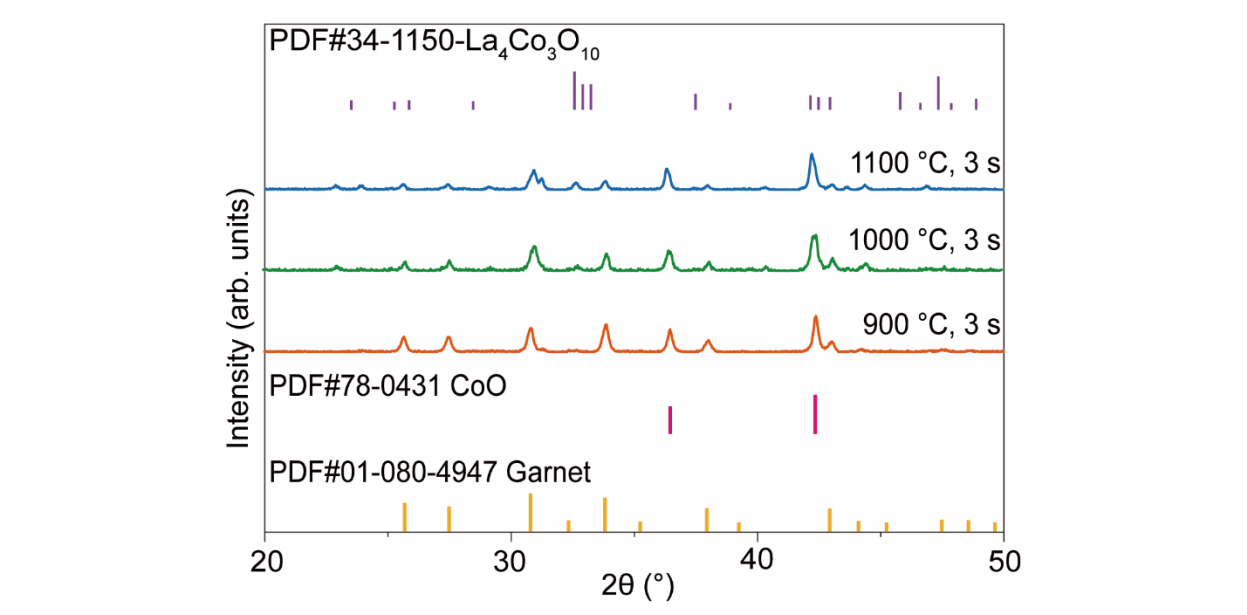

Supplementary Figure 17. XRD patterns of LLZTO and CoO heated by UHS. CoO and LLZTO maintain chemically stable at 1000 ℃ for 3 s.

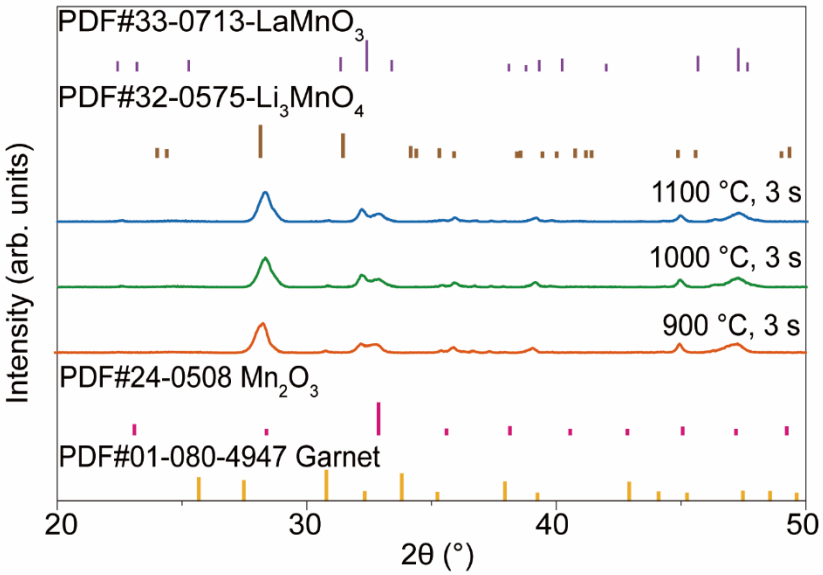

Supplementary Figure 18. XRD patterns of LLZTO and Mn_2O_3 heated by UHS. The impurity phases including Li_3MnO_4 and $LaMnO_3$ are formed at 900 ℃ for 3 s.

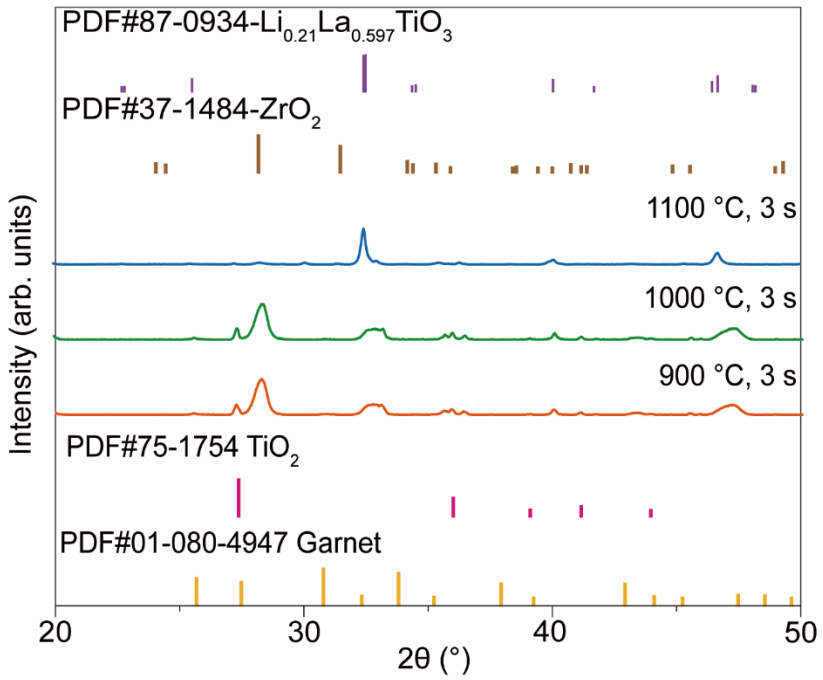

Supplementary Figure 19. XRD patterns of LLZTO and TiO_2 heated by UHS. The side reactions occur at 900 ℃ for 3 s.

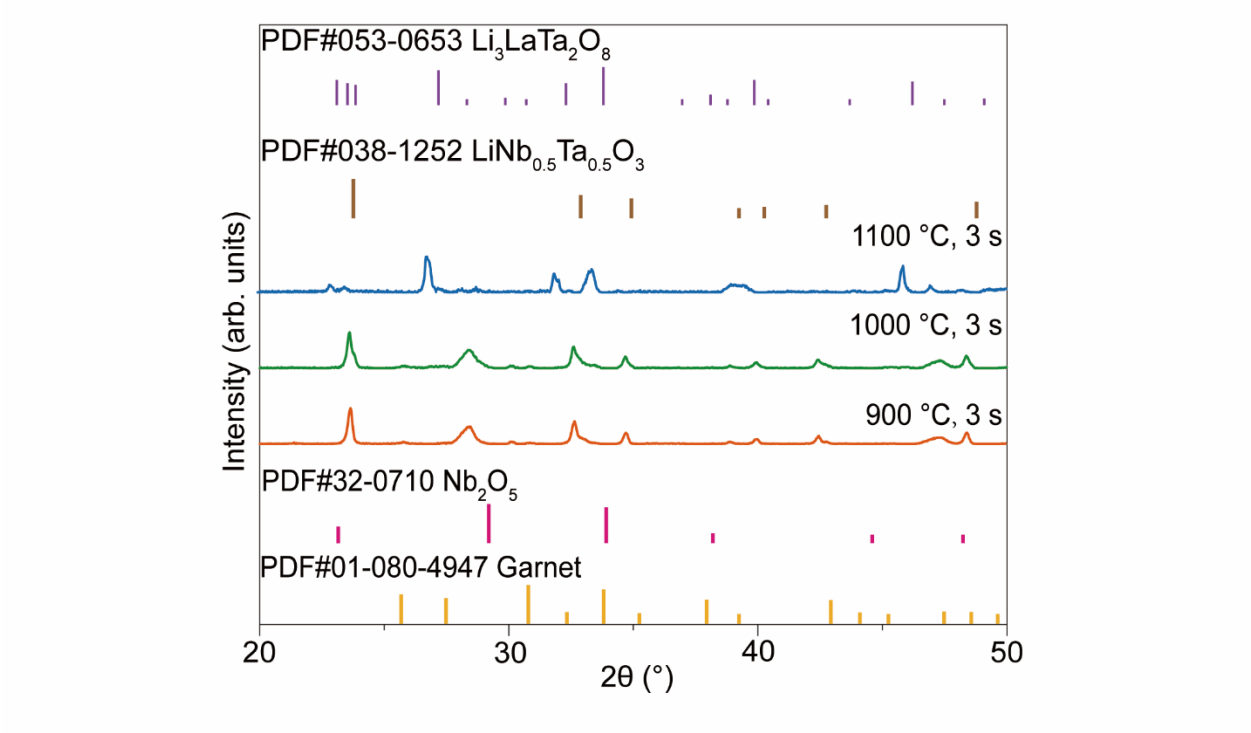

Supplementary Figure 20. XRD patterns of LLZTO and Nb_2O_5 heated by UHS. The side reactions occur and the impurity phases ($LiNb_{0.5}Ta_{0.5}O_3$, $Li_3LaTa_2O_8$) are formed at 900 ℃ for 3 s.

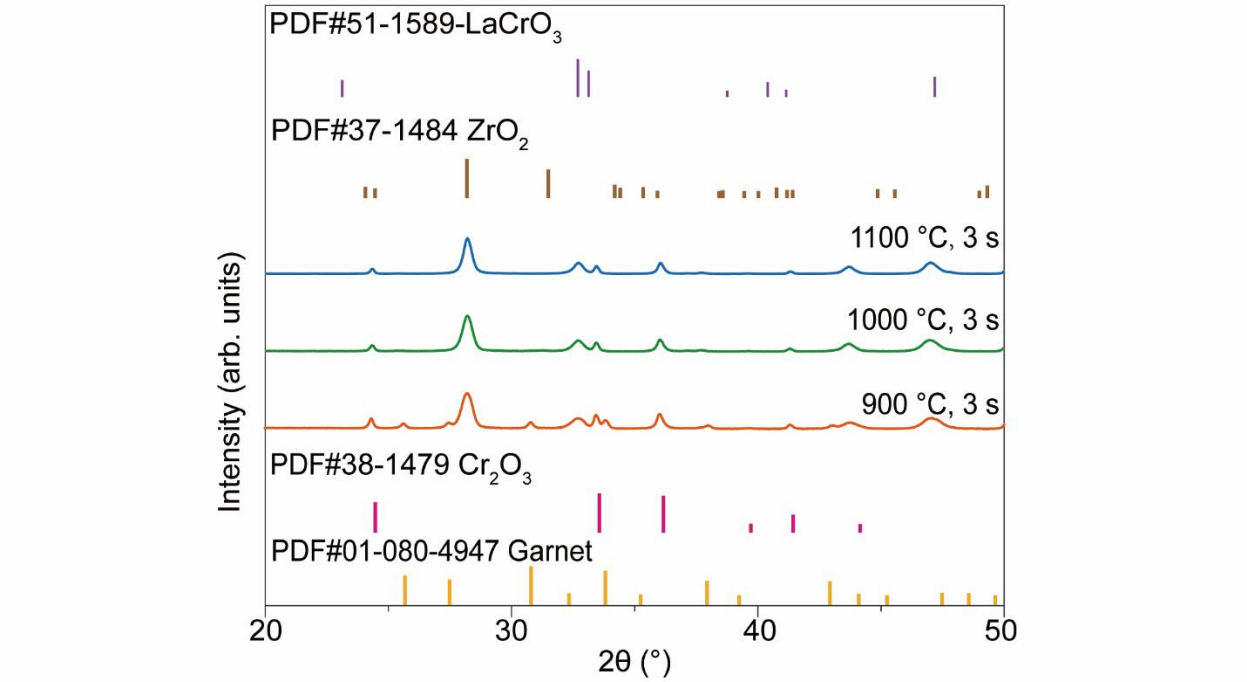

Supplementary Figure 21. XRD patterns of LLZTO and Cr_2O_3 heated by UHS. The side reactions occur and the impurity phases ($LaCrO_3$, ZrO_2) are formed at 900 ℃ for 3 s.

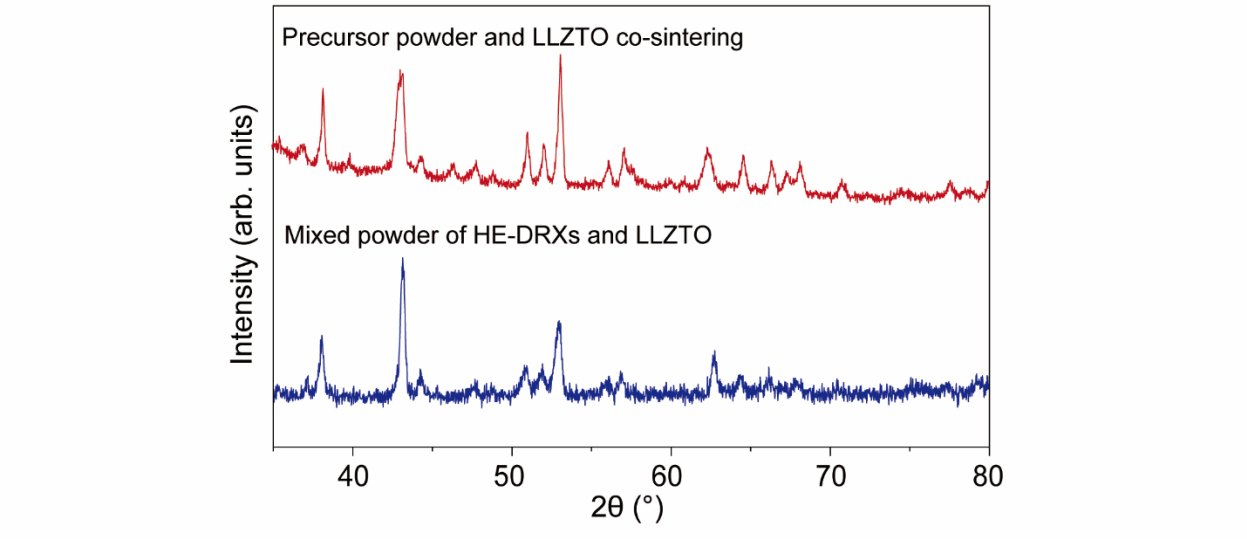

Supplementary Figure 22. XRD patterns of LLZTO and the precursor powder of HE-DRXs co-sintered at 1100 ℃ for 3 s by UHS.

Supplementary Table 2. Thermodynamically Possible Reaction Products between each individual component of HE-DRXs and LLZTO.

Oxide	MnO	CoO	Cr_2O_3	TiO_2	Mn_2O_3	Nb_2O_5
Reaction products	not react	$Li_{10}Co_4O_9$, $Li_6Zr_2O_7$, La_2O_3	$LaCrO_3$, $LiCrO_2$, $La_2Zr_2O_7$	Li_2TiO_3, La_2TiO_5, $La_2Zr_2O_7$	$LiMnO_2$, Li_2ZrO_3, $La_5Mn_5O_{16}$, MnO	Li_3NbO_4, $LaNbO_4$, ZrO_2
Reaction energy (meV/atom)	not react	-3.08	-87	-104	-118	-135

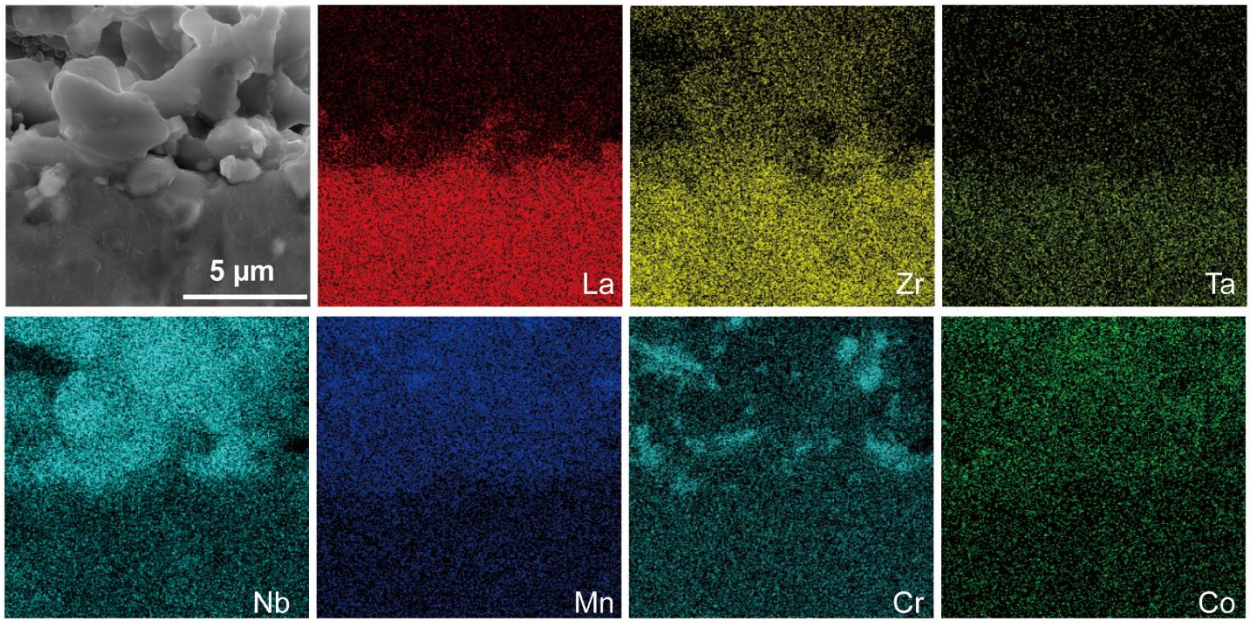

Supplementary Figure 23. SEM–EDS images of the TM6|LLZTO interface. The short reaction time of 3 s effectively suppresses element diffusion and delays the occurrence of side reactions between HE-DRXs and LLZTO.

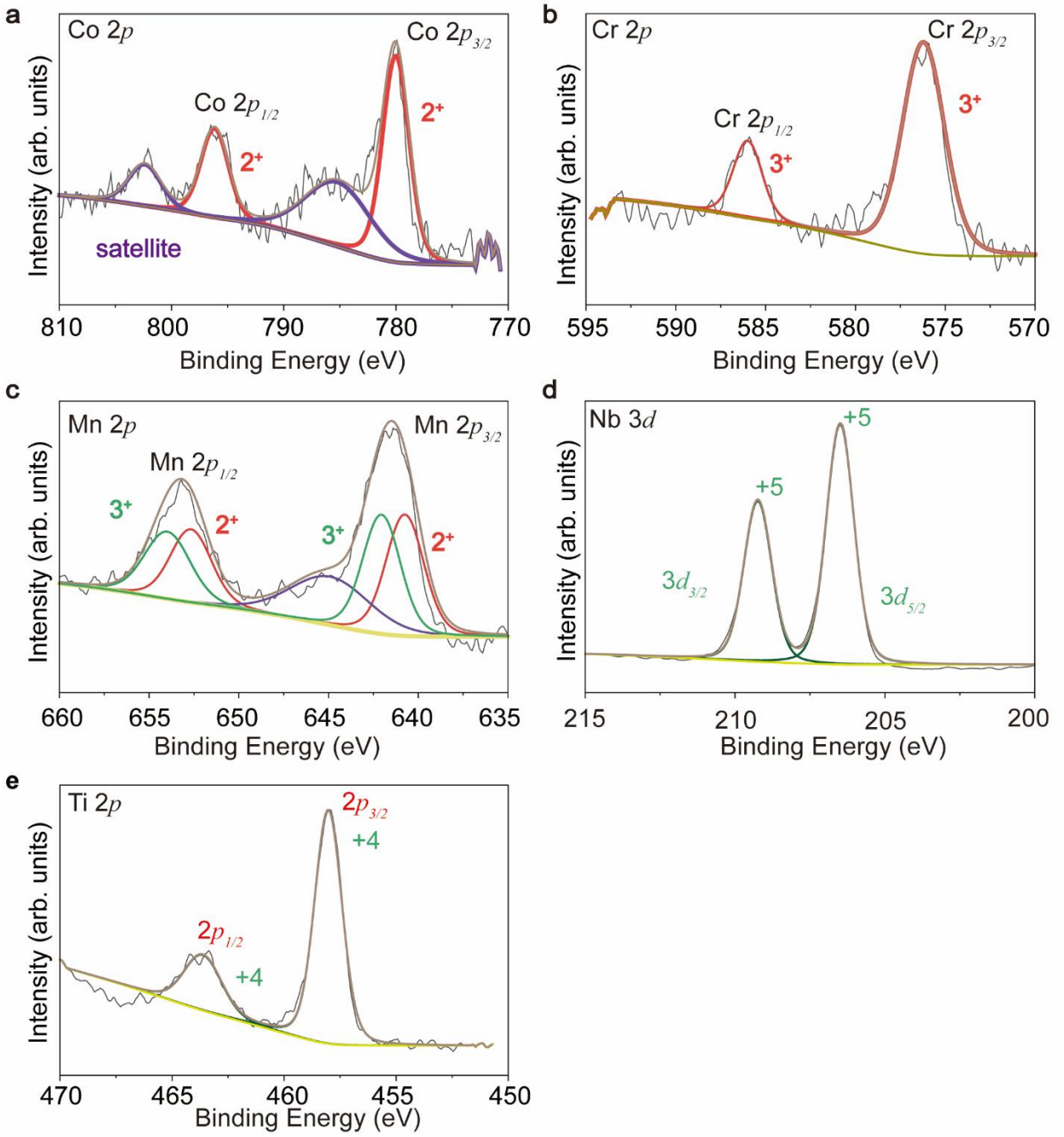

Supplementary Fig. 24. XPS spectra of (a) Co2p, (b) Cr 2p, (c) Mn 2p, (d) Nb 3d and (e)Ti 2p of the in situ synthesized TM6 by UHS. Mn can exist in both +2 and +3 valence states. Co is in the +2 valence state, while Cr is in the +3 valence state. Ti and Nb, which are utilized to stabilize the positive electrode framework, exhibit oxidation states of +4 and +5, respectively.

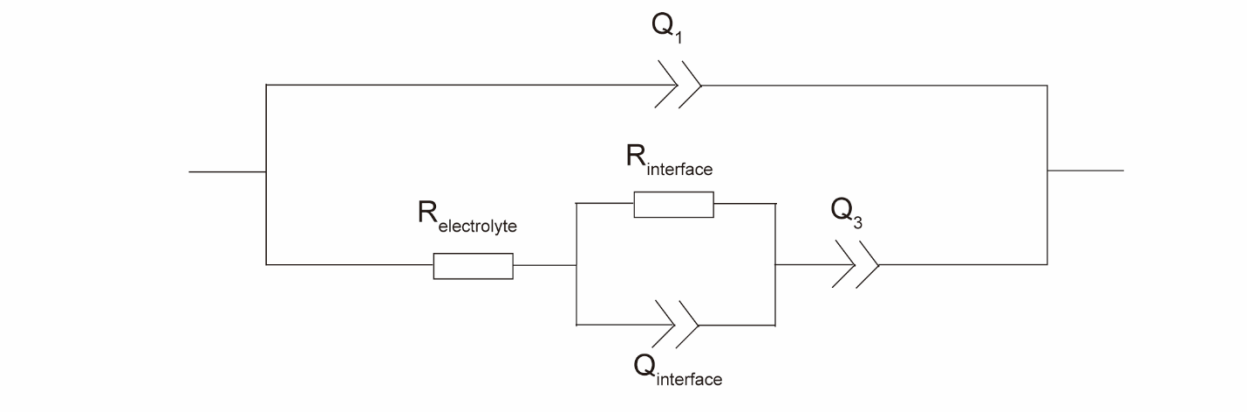

Supplementary Fig. 25. Equivalent circuit for determining ionic conductivity of symmetric cells using the Li^+ blocking configuration (Au|Positive electrode|LLZTO|Positive electrode|Au)[1].

By analyzing the EIS fitting curves of symmetric cells, the conductivity of LLZTO was determined to be 4.08×10^{-4} S/cm for Au|TM6|LLZTO|TM6|Au and 2.77×10^{-4} S/cm for Au|$LiCoO_2$|LLZTO|$LiCoO_2$|Au, which aligns well with the reported conductivity values for LLZTO in the literature. This consistency further confirms the accuracy of the employed equivalent circuit **(Supplementary Fig. 24)**.

Based on the fitting data presented in **Table S2** and **Table S3**, the calculated area-specific resistance (ASR) at the interface of TM6|LLZTO is 31.6 $\Omega \cdot cm^2$, while that of the $LiCoO_2$|LLZTO interface is 23175.5 $\Omega \cdot cm^2$. The ASR of the TM6|LLZTO interface is approximately 700 times lower than that of the $LiCoO_2$|LLZTO interface. This significant difference indicates a substantially reduced resistance at the TM6|LLZTO interface compared to the $LiCoO_2$|LLZTO interface.

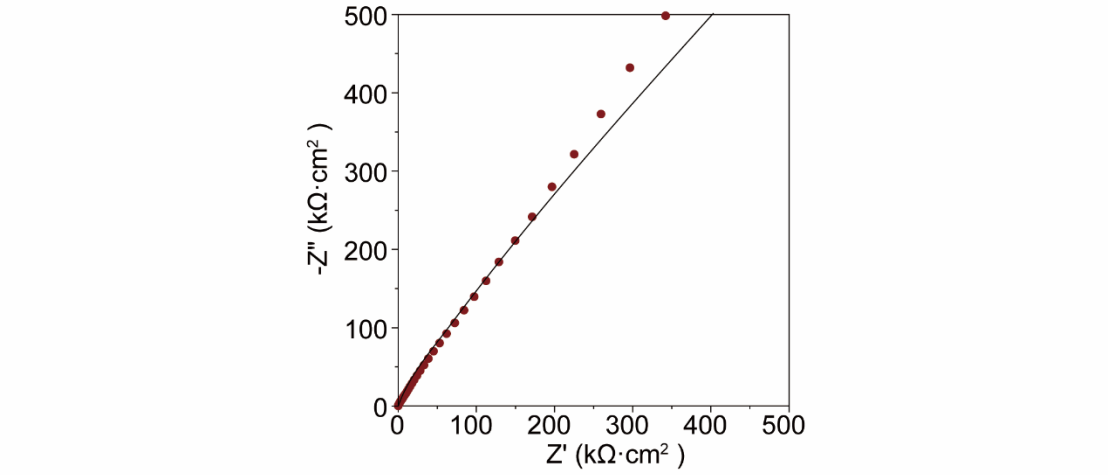

Supplementary Fig. 26. EIS of the TM6|LLZTO symmetric cell after rapid annealing by the UHS method, tested at 25 ℃.

Supplementary Table 3. Fit values for EIS spectra using the equivalent circuits (Au|TM6|LLZTO|TM6|Au).

$Q_1/(R_{LLZTO} + R_{interface}/Q_{interface} + Q_3)$	Value	Unit
Q_1	0.5162×10^{-6}	F.s^(a-1)
a_1	0.4651	
R_{LLZTO}	319.6	Ohm
$R_{LLZTO\|TM6\ interface}$	85.87	Ohm
$Q_{LLZTO\|TM6\ interface}$	3.676×10^{9}	F.s^(a-1)
$a_{LLZTO\|TM6\ interface}$	0.4922	
Q_3	0.2135×10^{-6}	F.s^(a-1)
a_3	0.766	

Supplementary Table 4. Fit values for EIS spectra using the equivalent circuits (Au|LCO|LLZTO|LCO|Au).

$Q_1/(R_{LLZTO} + R_{interface}/Q_{interface} + Q_3)$	Value	Unit
Q_1	9.277×10^{-15}	F.s^(a-1)
a_1	0.3556	
R_{LLZTO}	534.7	Ohm
$R_{LLZTO\|LCO\ interface}$	68668	Ohm
$Q_{LLZTO\|LCO\ interface}$	0.4494×10^{-6}	F.s^(a-1)
$a_{LLZTO\|LCO\ interface}$	0.7997	
Q_3	3.905×10^{-6}	F.s^(a-1)
a_3	0.4851	

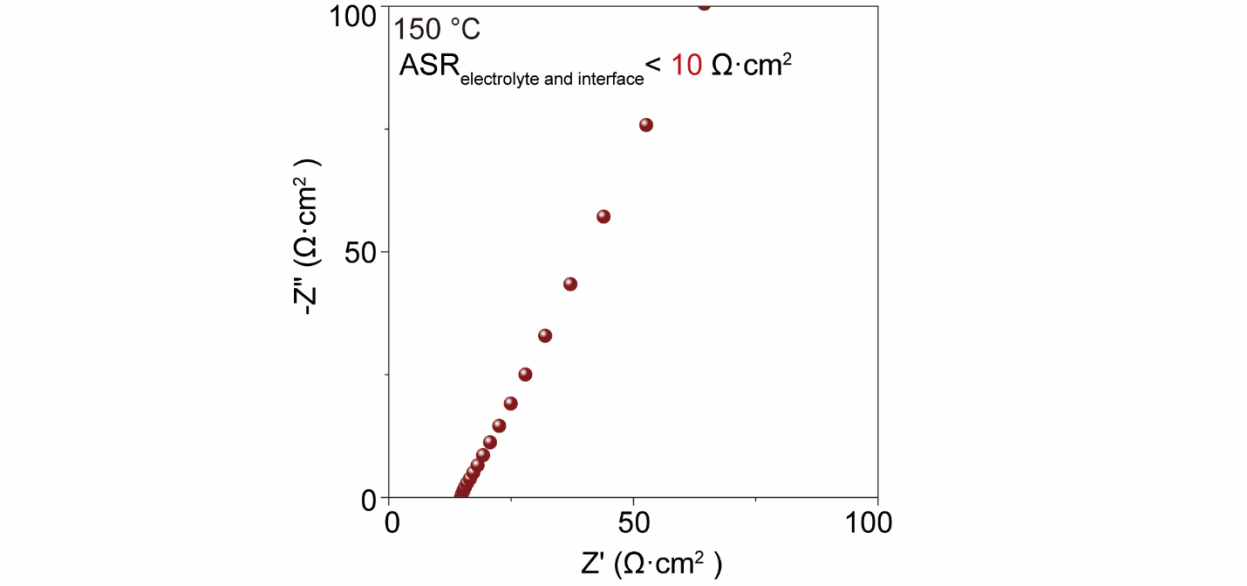

Supplementary Figure 27. EIS of the HE-DRXs|LLZTO symmetric cell after rapid annealing by the UHS method, tested at 150 ℃.

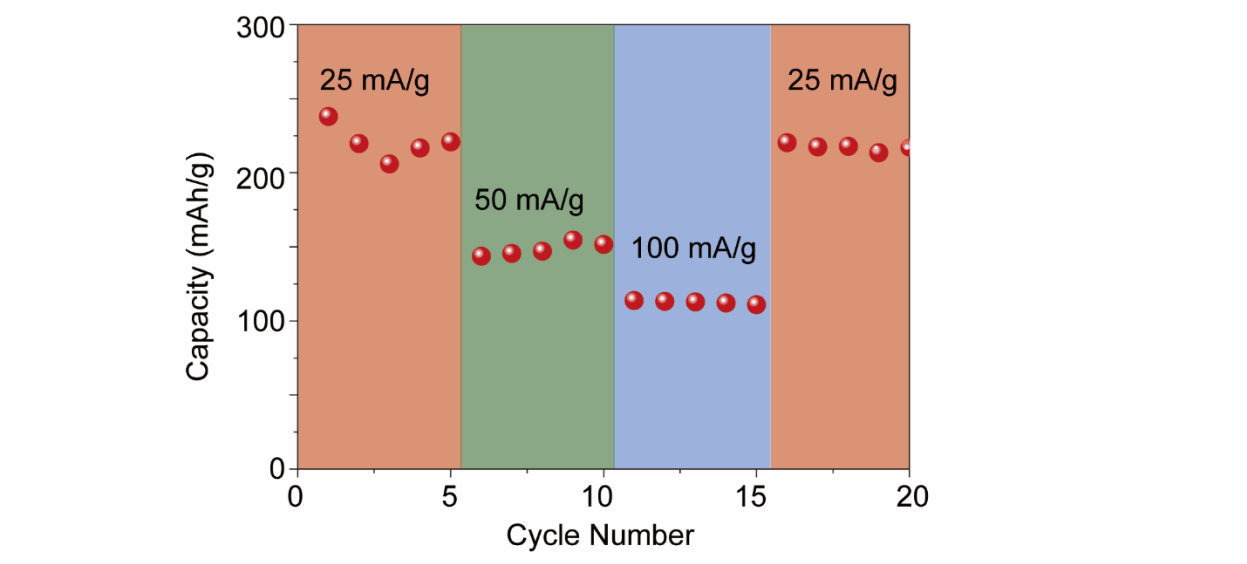

Supplementary Figure 28. Rate performance of the HE-DRXs-ASSLBs.

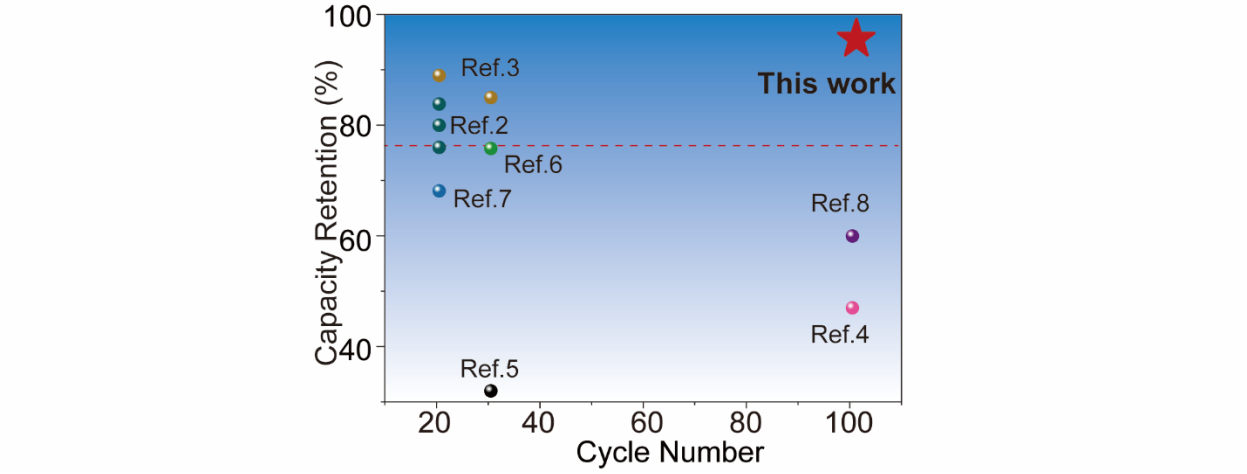

Supplementary Figure 29. Comparison of the capacity retention of DRXs in the literature[2–8].

Supplementary Table 5. Electrochemical performance of LLZO-based all-solid-state batteries.

Study	Positive electrode Composition	Proportion of active substance	Temperature	Loading (mg/cm^2)	Current	Voltage Range (V)	Capacity (mAh/g)	No. of Cycles	Capacity retention
Ref.[9]	LCO-LLZTO	50%	80 ℃	N/A	50 $\mu A/cm^2$	3.4-4.2	N/A	60	33.3%
Ref.[10]	Li_3BO_3@LCO +LLZO+ITO	60%	80 ℃	1	0.1C (14 mA/g)	3.0-4.1	101	40	66%
Ref.[11]	LCO+Li_3BO_3 +LLZO (42:35:23)	42%	25 ℃	N/A	0.01 C (1.4 mA/g)	3.0-4.2	78	1	N/A
Ref.[12]	$LiNi_{0.6}Mn_{0.2}Co_{0.2}O_2$	100%	80 ℃	N/A	0.5C (70 mA/g)	3.0-4.2	77	10	< 79%
Ref.[13]	LCO + porous LLZO scaffold (3:10)	23%	80 ℃	0.73	0.05 C (7 mA/g)	3.0-4.05	118	14	97%
Ref.[14]	LCO@Li_2CO_3 + LLZO@Li_2CO_3+ $Li_{2.3}C_{0.7}B_{0.3}O_3$ (58:30:12)	58%	100 ℃	1	0.05C (7 mA/g)	3.0-4.05	106	40	66%
Ref.[15]	V_2O_5+ CNT (9:1)	90%	100 ℃	0.2	50 mA/g	1.2-4.5	150	27	83.3%
Ref.[16]	LCO+LLZO	60%	60 ℃	2	25 mA/g	2.8-3.6	110	5	71%
Ref[17].	LCO+LLZO	N/A	80 ℃	16	3 mA/g	2.8-3.4	75	5	66.7%
Ref.[18]	LCO+LLZTO	50%	50 ℃	12.6	4 mA/g	2.4-3.6	110	100	27.6%
This work	HE-DRXs +LLZTO (5:1)	83.33%	150 ℃	1.3	25 mA/g	1.7-4.7	**238**	**100**	**95%**

Supplementary References

1. Huggins, R. A. Simple method to determine electronic conductivity and ionic components of the conductors in mixed a review. *Ionics* **8**, 300–313 (2002).
2. Lun, Z. *et al.* Cation-disordered rocksalt-type high-entropy cathodes for Li-ion batteries. *Nature Materials* **20**, 214–221 (2021).
3. Lun, Z. *et al.* Design Principles for High-Capacity Mn-Based Cation-Disordered Rocksalt Cathodes. *Chem* **6**, 153–168 (2020).
4. House, R. A. *et al.* Lithium manganese oxyfluoride as a new cathode material exhibiting oxygen redox. *Energy and Environmental Science* **11**, 926–932 (2018).
5. Kan, W. H. *et al.* Evolution of Local Structural Ordering and Chemical Distribution upon Delithiation of a Rock Salt–Structured Li 1.3 Ta 0.3 Mn 0.4 O 2 Cathode. *Advanced Functional Materials* **29**, 1–11 (2019).
6. Wang, R. *et al.* Research on the kinetic properties of the cation disordered rock-salt Li-excess Li1.25Nb0.25Mn0.5O2 material. *Solid State Ionics* **339**, 114999 (2019).
7. Wang, M. *et al.* Research Progress in Lithium-Excess Disordered Rock-Salt Oxides Cathode. *Energy and Environmental Materials* **5**, 1139–1154 (2022).
8. Kitchaev, D. A. *et al.* Design principles for high transition metal capacity in disordered rocksalt Li-ion cathodes. *Energy and Environmental Science* **11**, 2159–2171 (2018).
9. Kato, T. *et al.* In-situ Li7La3Zr2O12/LiCoO2 interface modification for advanced all-solid-state battery. *Journal of Power Sources* **260**, 292–298 (2014).
10. Ramkumar, B., So-young, K., Chan-woo, N., Aravindan, V. & Yun-Sung, L. LiBO2-modified LiCoO2 as an efficient cathode with garnet framework

Li6.75La3Zr1.75Nb0.25O12 electrolyte toward building all-solid-state lithium battery for high-temperature operation. *Electrochimica Acta* **359**, 136955 (2020).

11. Ohta, S. *et al.* Co-sinterable lithium garnet-type oxide electrolyte with cathode for all-solid-state lithium ion battery. *Journal of Power Sources* **265**, 40–44 (2014).
12. Kim, Y., Waluyo, I., Hunt, A. & Yildiz, B. Avoiding CO2 Improves Thermal Stability at the Interface of Li7La3Zr2O12 Electrolyte with Layered Oxide Cathodes. *Advanced Energy Materials* **12**, 2102741 (2022).
13. Kim, K. J. & Rupp, J. L. M. All ceramic cathode composite design and manufacturing towards low interfacial resistance for garnet-based solid-state lithium batteries. *Energy and Environmental Science* **13**, 4930–4945 (2020).
14. Han, F. *et al.* Interphase Engineering Enabled All-Ceramic Lithium Battery. *Joule* **2**, 497–508 (2018).
15. Liu, B. *et al.* Rapid thermal annealing of cathode-garnet interface toward higherature solid state batteries. *Nano Letters* **17**, 4917–4923 (2017).
16. Scheld, W. S. *et al.* Rapid thermal processing of garnet-based composite cathodes. *Journal of Power Sources* **545**, (2022).
17. Ihrig, M. *et al.* Low temperature sintering of fully inorganic all-solid-state batteries – Impact of interfaces on full cell performance. *Journal of Power Sources* **482**, (2021).
18. Tsai, C. L. *et al.* A garnet structure-based all-solid-state Li battery without interface modification: Resolving incompatibility issues on positive electrodes. *Sustainable Energy and Fuels* **3**, 280–291 (2019).